Energy Advances

ROYAL SOCIETY OF CHEMISTRY

PAPER

View Article Online
View Journal | View Issue

Cite this: *Energy Adv.*, 2024, 3, 654

An *in situ* formed ZIF-67 derived NiFeCo-P nano-array for accelerating the electrocatalytic oxygen evolution reaction†

Xi Guo, Li Li,* Shuo Wang, Huan Zhang, Yuzhen Kuang, Guangbin Duan* and Bingqiang Cao

Received 28th November 2023,
Accepted 11th February 2024

DOI: 10.1039/d3ya00581j

rsc.li/energy-advances

In situ growth of nano-arrays on substrate materials is a neoteric and efficacious catalyst design strategy, but it is still a difficulty to prepare unique nano-structured electrocatalysts with excellent activity for the oxygen evolution reaction (OER). In this study, phosphidizating ternary nickel/iron/cobalt hybrid nano-arrays (NiFeCo-P) with vertically staggered growth were successfully synthesized on the surface of nickel foam (NF) through three steps: impregnation, hydrothermal reaction and phosphidizating calcination. The initial ZIF-67/NF and the derived NiFeCo-layered double hydroxide (LDH)/NF nano-array (NiFeCo-LDH/NF) template promote the charge transfer and ion diffusion between electrolyte surfaces, which is attributed to the enhancement of the interface contact area of electrolyte ions. Phosphidizated NiFeCo-LDH/NF nano-arrays (NiFeCo-P/NF) showed lower overpotential of 251 and 278 mV at 50 mA cm^{-2} and 100 mA cm^{-2}, respectively. The Tafel slope was 25.24 mV dec^{-1}, which was better than the performance of some transition metal-based OER catalysts reported before. Electrochemical impedance spectroscopy further revealed the good kinetics in the electrolysis process. Furthermore, the high structural stability of the nanosheet array promotes the generation of the active phase in the OER process, so it has good stability after continuous operation for 20 h at a current density of 50 mA cm^{-2}.

Introduction

In recent years, the energy crisis has been worsening and the environment has been gradually destroyed.[1] Hydrogen (H_2) is regarded as an ideal energy source because of its clean and renewable characteristics.[2] As one of the production methods of hydrogen, electrocatalytic water-splitting has become very attractive.[3] The oxygen evolution reaction (OER), however, is a slow four-electron kinetic reaction, which occurs far from the equilibrium (1.23 V *vs.* RHE).[4,5] Therefore, the OER is considered by the public as the bottleneck of the practical application of electrocatalytic hydrogen production. Designing high-performance OER electrocatalysts is an effective way to reduce the overpotential and elevate the energy conversion efficiency. At present, the expensive iridium-based and ruthenium-based electrocatalysts are well known as the most effective OER catalytic materials.[6] However, their high prices and low abundance limit large-scale production.

In order to realize the sustainable development of industrialization, in recent years, many non-noble metal-based electrocatalysts with high efficiency, environmental protection, low-budget and abundant reserves have been applied to electrocatalytic water cracking, one of which involves improving the OER activity. Monumental efforts have been made to design and prepare diversiform transition metals and their derivatives, such as transition metal-based oxides,[7] carbides,[8] nitrides,[9] phosphides,[10] sulfides,[11] selenides,[12] borides[13] and other electrocatalysts[14] for the OER.

Transition metal phosphide (TMP) is a candidate with great promise in OER catalytic materials, which exhibits relatively high catalytic OER activity and conductivity.[15] Phosphidizating treatment may lead to lattice distortion and charge redistribution, which is beneficial to regulate the electronic structure of electrocatalysts and reinforce their electrocatalytic performances.[16] For instance, Zhang *et al.* prepared 3D hierarchical heterostructure NiFe LDH@NiCoP/NF electrodes, which exhibited an overpotential of 220 mV at 10 mA cm^{-2} for the OER.[17] Wang *et al.* loaded a 3D heterostructure NiCoP@NiMn-layered double hydroxide array on Ni foam, and its OER overpotential was 293 mV at 100 mA cm^{-2}.[18] Yang *et al.* successfully synthesized a unique nanostructured catalyst by *in situ* growth of Mo-doped Ni_2P ultrafine nanosheets with NiFe LDH nanosheets as the skeleton, with an overpotential

School of Materials Science and Engineering, University of Jinan, Jinan 250022, Shandong, China. E-mail: mse_lil@ujn.edu.cn

† Electronic supplementary information (ESI) available. See DOI: https://doi.org/10.1039/d3ya00581j

of 269 mV at 40 mA cm^{-2}.[19] Li *et al.* prepared a layered hetero-carbon structure by coating Ni–Co LDH ultrathin nanosheets on cobalt phosphide nanosheet arrays (Co_xP@NiCo-LDH).[20] In the mixed electrolyte 1.0 M KOH, the potentials required an over-potential of 269 mV in 40 mA cm^{-2}. Although it is very necessary, it is still a very challenging task to construct TMP catalysts with a well-designed surface microstructure to achieve high active site exposure.

Metal–organic frameworks (MOFs) are microporous and mesoporous crystal materials formed by coordination bonds between metal ions and organic ligands.[21] In the past few decades, due to their extremely high surface area and pore volume and adjustable structure and composition, various applications have been studied, including supercapacitors,[22] gas sensing,[23,24] electrocatalysis,[25] adsorption[26] and biomedicine.[27] Zeolite imidazolate framework-67 (ZIF-67) has been widely used as a classical MOF for the OER. ZIF-67 has outstanding advantages in building multifunctional nano-arrays with nano-size and oriented arrangement. Its porous nanoarray creates an open environment for obtaining a large number of active sites and free transfer of active substrates,[28] which can provide an ideal molecular platform for designing and synthesising highly active TMP catalysts.

This article reports an inherent route for preparing phosphidizated NiFeCo-LDH/NF nano-array electrocatalysts with a sheet-like structure using a template method. Using the method of pre-growing ZIF-67 on NF, cobalt can be doped into the subsequently grown NiFe-LDH nanosheets, and NiFeCo-LDH/NF with a regularly arranged nanoflake array is obtained, which provides a template for the subsequently derived NiFeCo-P/NF. After phosphidization, the NiFeCo-P nanosheet array grows uniformly on NF, and shows excellent electrocatalytic activity for the OER (the overpotentials at 50 and 100 mA cm^{-2} are 251 and 278 mV, respectively). More importantly, it exhibits excellent stability at 50 mA cm^{-2}, lasting for 20 hours. The interesting point of this work is that the ZIF-67 nano-array was used as the starting material to manufacture the ideal LDH nano-array, thus obtaining a ternary hybrid nano-array with the synergistic effect of the nanosheet network and ternary mixed metals, and providing an ideal platform for further phosphorylation. Phosphidization further regulates the electronic structure of the electrocatalyst, accelerates electron transfer and helps to promote the OER. Therefore, it has become a promising OER electrocatalyst to replace precious metals.

Experimental

Materials

Nickel(II) nitrate hexahydrate ($Ni(NO_3)_2{\cdot}6H_2O$, 99%), cobalt(II) nitrate hexahydrate ($Co(NO_3)_2{\cdot}6H_2O$, 99%) and potassium hydroxide (KOH, 95%) were obtained from Shanghai Macklin Biochemical Co., Ltd. 2-Methylimidazole (98%) was obtained from Shanghai Aladdin Biochemical Technology Co., Ltd. Iron(III) nitrate nonahydrate ($Fe(NO_3)_3{\cdot}9H_2O$, 99%) and ammonium fluoride (NH_4F, $\geq$96%) were obtained from Sinopharm Chemical Reagent Co., Ltd. Urea ($\geq$99%) were purchased from Tianjin Damao Chemical Reagent Co., Ltd. Hydrochloric acid (HCl) and acetone (C_2H_6O, 99.5%) were purchased from Yantai Yuandong Fine Chemicals Co., Ltd. Anhydrous ethanol (CH_3CH_2OH, $\geq$99.7%) was purchased from Tianjin Fuyv Fine Chemicals Co., Ltd. All chemicals were of analytical grade and used as received without any further purification. Deionized (DI) water was used throughout the experiment.

The preparation of ZIF-67/NF

2-Methylimidazole (12 mmol, 0.985 g) and $Co(NO_3)_2{\cdot}6H_2O$ (1.5 mmol, 0.436 g) were dissolved in 30 mL deionized water, respectively, and recorded as solution A and solution B. After solution A and solution B were stirred for 15 minutes, respectively, solution A was quickly poured into solution B, and the stirring was continued for 5 minutes. Subsequently, the pre-washed nickel foam (NF, 3 × 2 cm) was immersed in the mixed solution for 4 hours. The prepared ZIF-67/NF was washed with deionized water and absolute ethanol and vacuum dried at 60 °C overnight.

The preparation of NiFeCo-LDH/NF

NiFeCo-LDH/NF was synthesized by a hydrothermal method. $Ni(NO_3)_2{\cdot}6H_2O$ (1 mmol, 0.290 g), $Fe(NO_3)_3{\cdot}9H_2O$ (0.2 mmol, 0.080 g), urea (7 mmol, 0.428 g) and NH_4F (3 mmol, 0.135 g) were dissolved in 25 mL deionized water. Then, a piece of ZIF-67/NF prepared above was transferred to a 50 mL Teflon-lined autoclave together with the above solution and maintained at 120 °C for 1 hour. Finally, NiFeCo-LDH/NF can be obtained by washing with anhydrous ethanol and deionized water and vacuum drying at 60 °C overnight. In addition, the cobalt element in NiFeCo-LDH/NF comes from ZIF-67. $Ni(NO_3)_2{\cdot}6H_2O$ and $Fe(NO_3)_3{\cdot}9H_2O$ were mixed in 25 mL deionized water to obtain mixed solutions with different Ni/Fe molar ratios, and the total amount of metal cations (Ni^{2+} and Fe^{3+}) was kept at 1.2 mmol.

The preparation of NiFeCo-P/NF

One porcelain boat containing 1 g NaH_2PO_2 was placed at the air inlet, and one porcelain boat containing NiFeCo-LDH/NF was put at the air outlet, with a distance of about 10 cm, and heated to 300 °C at a heating rate of 2 °C min^{-1} under the condition of introducing N_2. At about 300 °C, NaH_2PO_2 decomposes to generate PH_3, which is used for phosphorization of the LDH, as shown in eqn (1) and (2).[29] After cooling, the samples were collected, and the synthesized samples were marked as NiFeCo-P/NF. Comparatively speaking, NiFe-P/NF is obtained by combustion under the same conditions at 300 °C.

$$2NaH_2PO_2 \rightarrow Na_2HPO_4 + PH_3\uparrow \quad (1)$$

$$M^{2+} + PH_3 \rightarrow MmPn\ (M^{2+} = Ni^{2+}) \quad (2)$$

Material characterizations

Determination of the crystal structure of the product by X-ray diffraction (XRD, Rigaku SMARTLAB 9KW). Analysis of the micro-morphology of the sample was carried out by field-emission scanning electron microscopy (SEM, Zeiss QUANTA

FEG250) and transmission electron microscopy (TEM, Jeol JEM 2100). Exploration of the chemical valence state and special state of elements by X-ray photoelectron spectroscopy (XPS, Thermo ESCALAB Xi+).

Electrochemical measurements

A CHI660E electrochemical analyzer (ChenHua Instruments, Inc., Shanghai) was used for electrochemical measurements, and the test system is a three-electrode system. The electrolyte solution was 1.0 M KOH, and the test was carried out under the conditions of continuous stirring. The prepared samples (NiFeCo-P/NF, *etc.*, 1 × 1 cm), Pt sheet (1 × 1 cm) and Hg/HgO (1.0 M KOH, aqueous) were used as the working electrode, counter electrode and reference electrode, respectively. The potential drop (*iR*) losses caused by solution resistance and system resistance are applied to all the measured potentials (E_{mea}) to obtain the correction potential (E_{corr}), according to eqn (3):

$$E_{corr} = E_{mea} - iR \quad (3)$$

All related potentials are treated as the reversible hydrogen electrode (RHE) according to the following eqn (4).

$$E_{RHE} = E_{Hg/HgO} + 0.059 \times pH + 0.098\ V \quad (4)$$

The polarization curves of the electrocatalysts were obtained by linear sweep voltammetry (LSV) recording with a scanning rate of 1 mV s^{-1}. Moreover, electrochemical impedance spectroscopy (EIS) was acquired under the conditions of 1.5 V *vs.* RHE for the OER, respectively, from 10^5 to 0.01 Hz. In addition, the double-layer capacitance (C_{dl}) was calculated by cyclic voltammograms (CV) under different scan rates. All samples' electrochemical active surface area (ECSA) can be calculated by the equation:

$$ECSA = C_{dl}/C_s \quad (5)$$

where the value of C_s is 0.04 mF cm^{-2}, which corresponds to the specific capacitance in alkaline electrolyte.

The chronopotentiometry method was used to evaluate the stability of the electrocatalysts.

Results and discussion

Catalyst synthesis and structure characterization

The process for preparing the NiFeCo-P nano-array on NF is shown in Scheme 1. NF, as a 3D porous adhesive-free substrate, has sufficient mechanical strength and satisfactory conductivity. First, ZIF-67 was pre-grown on NF by the impregnation method. Then, considering that NiFe-LDH was the most promising alkaline OER electrocatalytic material to date, the NiFeCo-LDH/NF template with a layered nano-array was derived from ZIF-67/NF by the hydrothermal method. In order to optimize the electrochemical performance and conductivity, phosphorus was introduced into the electrocatalyst.[30] Thus, the NiFeCo-LDH/NF template was further converted into a NiFeCo-P/NF electrode. This unique and highly open nano-array network exposes abundant edge sites, thereby promoting mass transfer and boosting the electrocatalytic activity.[31] Meanwhile, NiFe-P/NF was prepared as a comparison.

SEM was used to investigate the morphology and structure of the catalyst. As can be seen from Fig. S1 (ESI†), the surface of NF is completely covered by the sandwich-shaped ZIF-67, and presents a regularly arranged nano-array, with a large open area. This provides a more suitable location for the growth of active substances, and the porous structure formed by the nanoarrays facilitates efficient mass transfer in the electrolysis reaction.[32] Since the satisfactory performance exhibited by the nickel-based electrocatalysts originates from the type of hydroxide produced during the electrochemical process, the introduction of Fe ions with similar atomic radius for Ni ions can enhance the catalytic performance of the nickel-based hydroxides.[33] From the SEM images (Fig. S2, ESI†), it can be seen that the domains of the nanosheets become smaller with the increase of the Ni/Fe ratio, and Ni, Fe, and O are uniformly distributed in the sheet NiFe-LDH/NF catalysts (Fig. S3, ESI†). As shown in Fig. S4 and S5 (ESI†), the electrocatalytic performances of the different samples were tested, and the composition with a Ni/Fe ratio of 5 : 1 exhibited excellent electrocatalytic activity. It can be seen that the synergistic effect of Ni and Fe can significantly promote the electrocatalytic performances.[34] Therefore, NiFe-LDH with a Ni/Fe ratio of 5 : 1 was grown on the ZIF-67/NF template to prepare the derivative NiFeCo-LDH

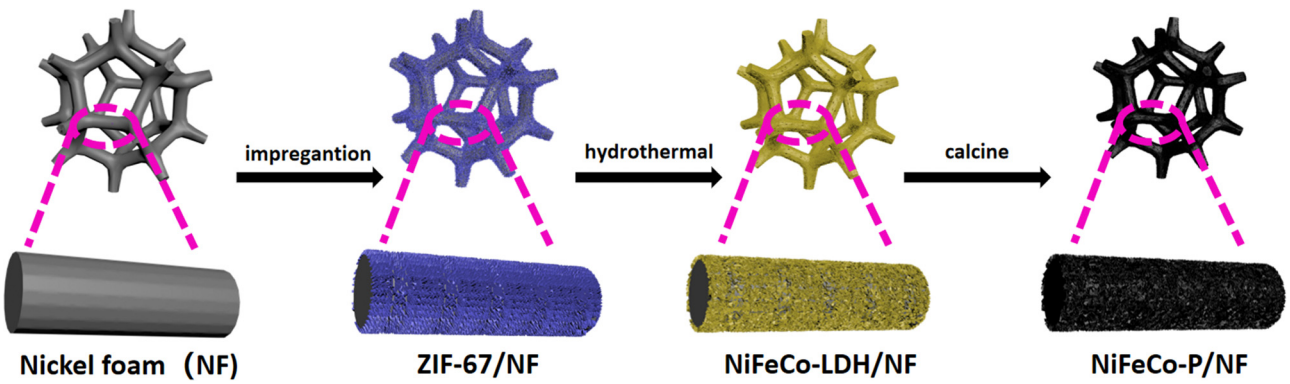

Scheme 1 Schematic illustration of the fabrication route of the NiFeCo-P/NF electrode.

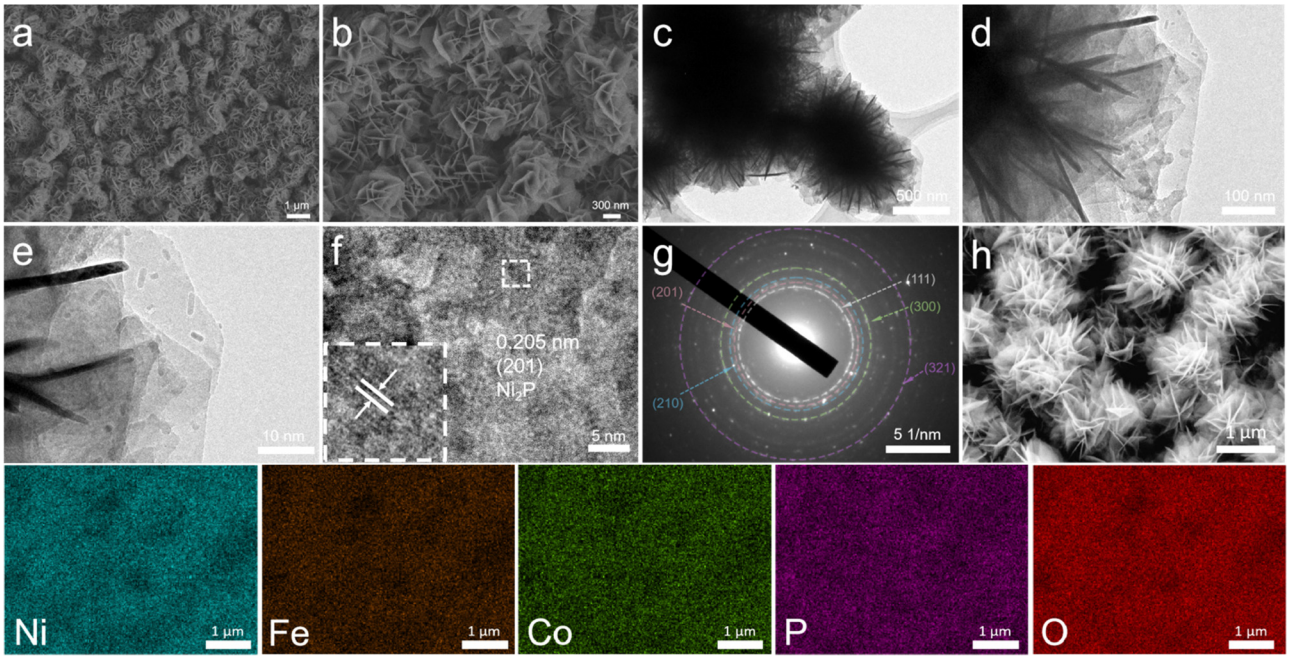

Fig. 1 (a) and (b) SEM images, (c)–(e) TEM images, (f) HRTEM image, and (g) SAED pattern of NiFeCo-P/NF. (h) SEM image and corresponding elemental mapping images of Ni, Fe, Co, P, and O elements.

electrocatalyst. Through high magnification SEM images, it can be observed that the sandwich structure on the original surface has been completely replaced by uniformly grown nanosheet nano-arrays (Fig. S6, ESI†).[35,36] The elemental distributions indicate that Ni, Fe, Co, and O are uniformly distributed in the NiFeCo-LDH/NF catalyst, and the elemental Co is successfully doped into the newly generated nanosheets (Fig. S7, ESI†). The introduction of cobalt cations with smaller atomic radii could improve the catalytic performance. As shown in Fig. 1a and b and Fig. S8 (ESI†), NiFeCo-P/NF and NiFe-P/NF still maintain the sheet-like structure of the nano-arrays after high-temperature phosphidization. TEM images of the nanosheets are shown in Fig. 1c–e, and they are almost transparent due to their ultra-thin nature. The high-resolution TEM (HRTEM) image (Fig. 1f) shows the well-resolved lattice stripes, and the plane spacing is 0.205 nm, which corresponds to the (201) plane of Ni_2P. The selected area diffraction pattern (SAED) in Fig. 1g also confirms the existence of Ni_2P. The elemental mapping images of NiFe-P/NF (Fig. S9, ESI†) and NiFeCo-P/NF (Fig. 1h) show that phosphorus was successfully introduced. This unique highly open network may expose abundant edge sites, thus promoting mass transfer and improving electrocatalytic activity.

In order to characterize the crystal structure of the synthesized samples, the corresponding XRD diagrams are shown in Fig. 2a and Fig. S10 (ESI†). Because of the strong diffraction peak of the Ni foam substrate, the diffraction peak of ZIF-67 is weak, and the XRD pattern of ZIF-67 is consistent with that described in the literature,[37] thus confirming the proper synthesis. In addition, there are three peaks at 44.46°, 51.81° and 76.33°, which belong to the (110), (200) and (220) crystal planes of Ni (JCPDS No. 04-0850) respectively.[38] After converting ZIF-67/NF into NiFeCo-LDH/NF by the hydrothermal method, we can see that the peak positions of the newly generated diffraction peaks can be classified as characteristic XRD patterns of the LDH phase (JCPDS No. 40-0215). The diffraction peaks at 11.53°, 23.28°, 34.56°, 39.01°, 60.28° and 61.25° can correspond to NiFe-LDH at (003), (006), (012), (015), (110) and (113).[39] And it can be seen that the intensity of the related diffraction peak of NiFeCo-LDH/NF is weaker than that of NiFe-LDH/NF, which may be caused by the doping of the Co element. After phosphidizating with NiFe-LDH/NF and NiFeCo-LDH/NF, it can be clearly observed that the LDH diffraction peaks disappear and the Ni_2P diffraction peaks appear after high temperature phosphidizating. The clear reflection of the Ni_2P phase indicates that the LDH precursor is successfully transformed into Ni–P phase. The diffraction peaks at 40.80°, 47.31°, 54.23° and 54.94° are well matched with the (111), (210), (300) and (211) planes of Ni_2P (JCPDS No. 03-0953).[19] The XRD results of NiFeCo-P/NF are completely consistent with the HRTEM analysis results. In addition, it is not possible to observe whether Fe and Co are phosphidizated or not in the XRD patterns because of the low content of Fe and Co elements in the nanosheets.

The chemical compositions and corresponding chemical bonding characteristics of NiFeCo-P/NF were explored by XPS. The survey spectrum (Fig. 2b) confirmed the existence of Ni, Fe, Co, P and O. It can be observed from Fig. 2c that the Ni 2p XPS spectrum of NiFeCo-P/NF has two peaks of spin orbit coupling origin at the binding energy values of 856.5 eV and 874.2 eV, corresponding to the Ni^{2+}.[40] In addition, there are two high energy peaks at 858.1 and 876.3 eV, which are related peaks of Ni^{3+}, and the other two higher energy peaks at 862.7 and 880.8 eV are mainly attributed to Ni 2p3/2 and Ni 2p1/2 satellite

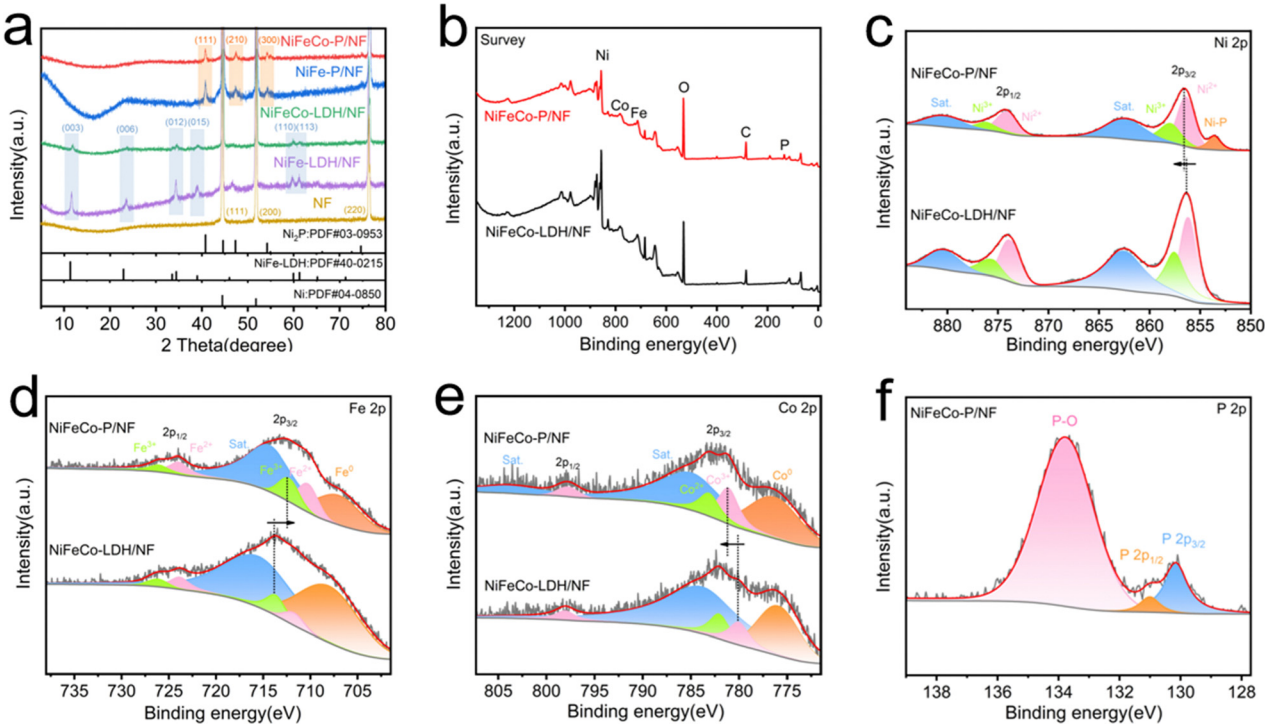

Fig. 2 (a) XRD patterns of NF, NiFe-LDH/NF, NiFe-P/NF, NiFeCo-LDH/NF and NiFeCo-P/NF. (b) XPS spectra of NiFeCo-LDH/NF and NiFeCo-P/NF. High-resolution XPS spectra of (c) Ni 2p, (d) Fe 2p and (e) Co 2p in NiFeCo-LDH/NF and NiFeCo-P/NF and of (f) P in NiFeCo-P/NF.

peaks, respectively.[40,41] $Ni^{\delta+}$ ($0 < \delta < 2$) in Ni–P leads to a peak at 853.6 eV, which proves the successful phosphidization.[29] The fitted Fe 2p spectrum (Fig. 2d) shows two Fe 2p3/2 peaks at 710.5 eV (Fe^{2+}) and 712.6 eV (Fe^{3+}), two Fe 2p1/2 peaks at 727.1 eV (Fe^{2+}) and 726.2 eV (Fe^{3+}), Fe^0, and related satellite peaks.[42] For the Co 2p spectrum shown in Fig. 2e, two major characteristic peaks at 781.2 and 783.3 eV were assigned to Co^{3+} and Co^{2+} of Co 2p3/2, and the peak at 798 eV was assigned to Co 2p1/2, respectively.[43] The P 2p spectrum is shown in Fig. 3f. There are two peaks for metal phosphide at 130.2 and 131.0 eV, and the peak at 133.8 eV can be attributed to PO_4^{3-}.[18] The XPS data of O 1s are shown in Fig. S11 (ESI†).[44] It is worth noting that the binding energy of Ni 2p shifted to a higher level, the binding energy of Fe 2p shifted to a lower level, and the binding energy of Co 2p shifted to a higher level, which may be related to the phosphidization of the material. Electronegativity P acts as a proton acceptor, causing changes in surface electronic structure and accelerating charge transfer.[45] Furthermore, the high valence states of Ni and Co can enhance absorption of the OH group during the electrocatalytic process and improve the OER performance. A similar phenomenon also exists in the XPS comparison of NiFe-LDH and NiFe-P (Fig. S12, ESI†).

Electrocatalytic performance

The electrocatalytic OER performances of the NiFeCo-P/NF nano-array were detected using a typical three-electrode electrolytic cell. For the convenience of comparison, bare NF, ZIF-67/NF, NiFe-LDH/NF, NiFe-P/NF, NiFeCo-LDH/NF and NiFeCo-P/NF nano-arrays were directly used as working electrodes and tested under the same conditions. After *iR* compensation, all measured potentials are referenced to RHE. Fig. 3a shows the polarization curve of NiFeCo-P/NF. The polarization curve shows that there is an oxidation peak between 1.3 and 1.5 V, which may correspond to the oxidation of M^{2+} to M^{3+} (M = Ni, Co), reported in NiFe LDH@NiCoP/NF and NiCoP@NiMn LDH/NF.[17,18] Among all electrocatalysts, NiFeCo-P/NF exhibits the highest electrocatalytic activity for the OER, while NiFeCo-LDH/NF, NiFe-P/NF, and NiFe-LDH/NF display relatively low electrocatalytic performance. The OER performance of the prepared samples was further evaluated by comparing the overpotential (Fig. 3b), and the NiFeCo-P/NF electrode required the smallest overpotentials of 251 and 278 mV at the current densities of 50 and 100 mA cm^{-2}, which is better than the NiFeCo-LDH/NF (254 and 285 mV), NiFe-P/NF (256 and 282 mV) and NiFe-LDH/NF electrodes (266 and 296 mV), respectively. After a careful literature search, the excellent OER performance of NiFeCo-P/NF is also better than that of some previous non-precious metal electrocatalysts (Fig. 3c), especially for operation at large current density ($\geq$100 mA cm^2).[18,43,46–57] In addition, Fig. 3d shows that the Tafel slope of NiFeCo-P/NF (25.24 mV dec^{-1}) is smaller than that of NiFeCo-LDH/NF (44.24 mV dec^{-1}), NiFe-P/NF (34.37 mV dec^{-1}) and NiFe-LDH/NF (52.83 mV dec^{-1}). The small Tafel slope of NiFeCo-P/NF indicates excellent electrocatalytic activity, because the rate of catalysis in the OER increases more significantly with the increase of the potential. Fig. 3e shows the Tafel diagram of the previously reported OER catalysts containing Ni_2P.[19,44,48,49,53,54,56,58–64] Obviously, the NiFeCo-P/NF catalyst exhibits excellent OER performance.

Electrochemical impedance spectroscopy (EIS) was used to study the charge transfer kinetics at the electrode interface. All EIS data (Fig. 3f) were fitted by using the equivalent circuit shown in ESI† Fig. S13, where R_s represents the resistance of the electrolyte, the electrocatalyst and all contact points, while R_{ct} represents the charge transfer resistance between catalyst and electrolyte, and the lower R_{ct} value represents a faster reaction rate. In addition, due to the porous surface of the electrode, the semicircle observed at higher frequency is related to R_t. According to the fitting diagram of EIS, NiFeCo-P/NF exhibits the smallest R_{ct} of 0.51 Ω compared with that of NiFeCo-LDH/NF (0.84 Ω), NiFe-P (0.90 Ω) and NiFe-LDH/NF (1.01 Ω), which indicates that NiFeCo-P/NF has excellent charge transfer ability. It is also the reason that NiFeCo-P/NF has low overpotential and small Tafel slope.

In order to further determine the possible influencing factors of excellent catalytic performance, samples were investigated through the C_{dl} getting from the CV curves (Fig. S5a and S14, ESI†) to evaluate the ECSA. Among them, the estimation of C_{dl} is carried out by linear fitting of different scanning rates and their capacitance current density differences at 0.05 V, and the fitting slope is twice that of C_{dl} (Fig. 3g). Compared with NiFeCo-LDH/NF (22.25 cm^2), NiFe-P/NF (52 cm^2), NiFe-LDH/NF (20.5 cm^2), and ZIF-67/NF (17.25 cm^2), NiFeCo-P/NF has a larger ECSA (58.75 cm^2), which mainly comes from the nano-array structure and more exposed active sites. The overpotential decrease of NiFeCo-P/NF can be attributed to the increase of ECSA compared with other samples studied in this work.

In addition to excellent OER activity, long-term durability is another criterion to assess the OER catalysts in large-scale industrial applications. The long-term chronopotentiometry of the NiFeCo-P/NF electrode was measured at a current density of 50 mA cm^{-2} for 20 hours, in order to evaluate the stability for the OER, and no degradation was observed (Fig. 3h). In addition, it

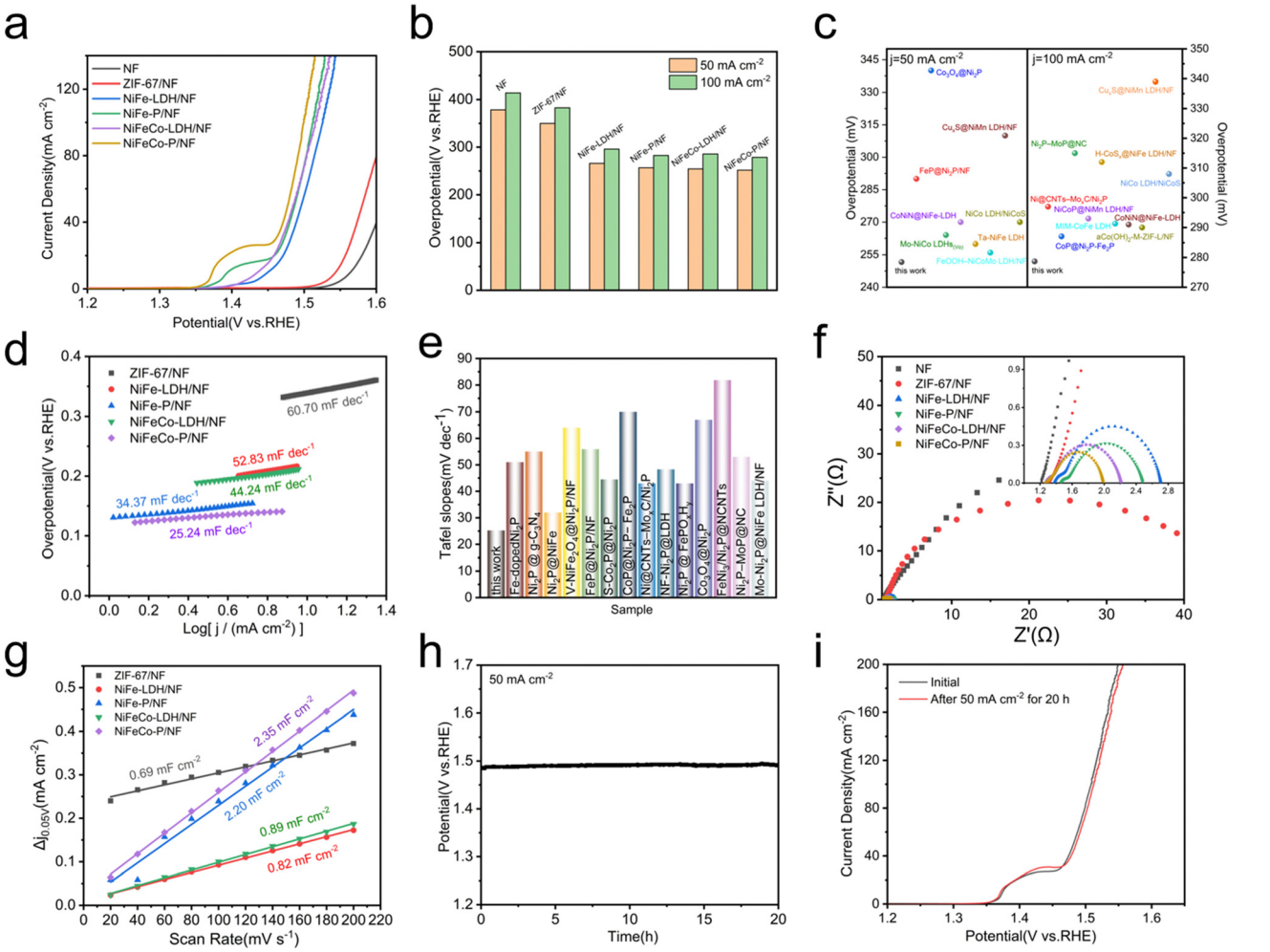

Fig. 3 (a) LSV curves, and (b) overpotentials at 50 and 100 mA cm^{-2} of NiFeCo-P/NF, NiFeCo-LDH/NF, NiFe-P/NF, NiFe-LDH/NF, ZIF-67/NF, and NF. (c) Comparisons of overpotential values of NiFeCo-P/NF with other reported catalysts. (d) Tafel slopes of NiFeCo-P/NF, NiFeCo-LDH/NF, NiFe-P/NF, NiFe-LDH/NF, and ZIF-67/NF. (e) Comparisons of the Tafel values of NiFeCo-P/NF with other reported catalysts. (f) EIS curves of NiFeCo-P/NF, NiFeCo-LDH/NF, NiFe-P/NF, NiFe-LDH/NF, ZIF-67/NF, and NF. (g) C_{dl} results of NiFeCo-P/NF, NiFeCo-LDH/NF, NiFe-P/NF, NiFe-LDH/NF, and ZIF-67/NF. (h) Chronopotentiometry curve for NiFeCo-P/NF at 50 mA cm^{-2}. (i) Polarization curves of NiFeCo-P/NF before and after the chronopotentiometry measurement.

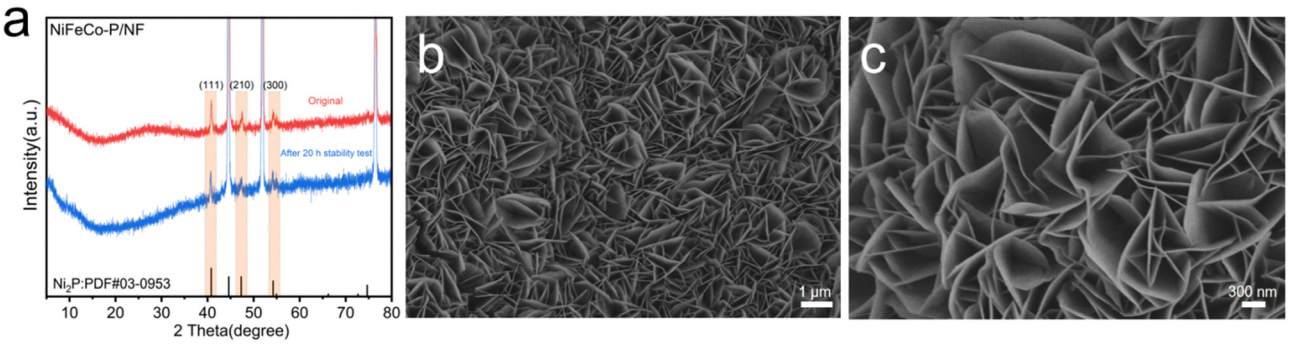

Fig. 4 (a) XRD pattern of the original NiFeCo-P/NF electrode and NiFeCo-P/NF electrode after the 20 h stability test. (b) and (c) SEM images of the NiFeCo-P/NF electrode after the 20 h stability test.

was observed from Fig. 3i that the polarization curve of NiFeCo-P/NF did not change significantly after 20 h chronopotentiometry measurement. Fig. S15 (ESI†) shows that the charge transfer resistance of NiFeCo-P/NF was slightly increased after the long-term stability test, which shows that NiFeCo-P/NF has good electrochemical stability. In conclusion, all of the results unquestionably indicate the outstanding OER activity and robust chemical stability of the NiFeCo-P/NF nano-array.

In order to further understand the stability of the material, the XRD diagram, SEM images and XPS spectra of NiFeCo-P/NF after the 20 h stability test have been compared. The electrode verified by XRD analysis in Fig. 4a has diffraction peaks similar to the original material, indicating that the crystal structure of the NiFeCo-P/NF electrode was well preserved, but the intensity of the diffraction peak was slightly weakened. On the other hand, after long-term stability testing, the morphology of the NiFeCo-P/NF nanosheets remains basically unchanged (Fig. 4b and c). In this case, Fig. 5a determines the decrease in P content. In addition, compared with the original sample, the high-resolution XPS spectra of the Ni 2p, Co 2p, Fe 2p, P 2p, and O 1s binding energies in the OER samples showed significant changes in intensity and peak position. From Fig. 5b, it can be seen that the high-resolution XPS Ni 2p spectrum shows a decrease in the Ni-P peak, while Ni 2p2/3 shifts negatively. The high-resolution XPS Fe 2p spectrum shows a positive shift in the characteristic peak (Fig. 5c). The high-resolution XPS Co 2p spectrum shows a negative shift in the characteristic peak (Fig. 5d). The weak P 2p spectrum of the sample after the 20 h stability test also recognizes a strong peak of the phosphidized component, while the phosphide portion is almost

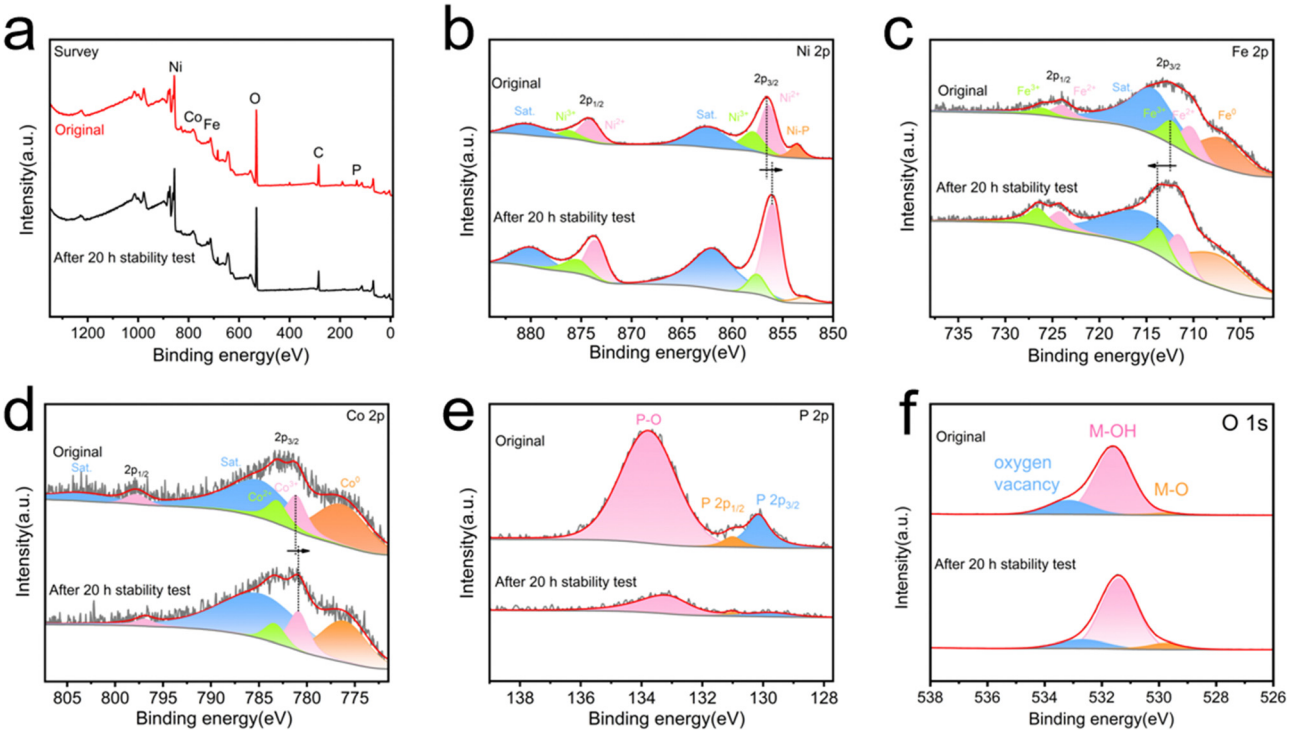

Fig. 5 (a) XPS survey spectra of the original and stability tested NiFeCo-P/NF electrode along with their high-resolution XPS spectra for (b) Ni 2p, (c) Fe 2p, (d) Co 2p, (e) P 2p, and (f) O 1s binding energies.

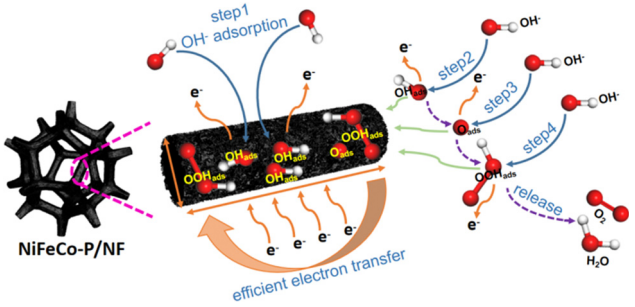

Fig. 6 Schematic illustration of NiFeCo-P/NF toward the OER in alkaline conditions.

invisible (Fig. 5e). Interestingly, the binding energy shift directions of Ni 2p, Fe 2p, and Co 2p are completely opposite to that after phosphidizating, further indicating that phosphidizating treatment regulates the electronic structure. In addition, the high-resolution XPS O 1s spectrum also showed an increase in peaks related to M–O bonds (Fig. 5f). The above XPS results indicate that during the OER process, the catalyst surface undergoes oxidation, which occurs in the form of oxide or (hydroxyl) oxide layers, which are also considered as electrocatalytic active phases.[65] At the same time, phosphorus also has the ability to act as a labile ligand, which can alter its coordination or chelation modes during the redox switching procedure of the metal ion and assist to promote the OER.[66] These results indicate that in the long-term OER reaction, the NiFeCo-P/NF catalyst of the electrode undergoes oxidation, but maintains the nanosheet structure and main crystal phase.

The proposed OER mechanism is shown in Fig. 6. Generally speaking, the OER process is a complex four-electron oxidation process. In the OER process, the functions of the active sites mainly include adsorbing basic substances (O*, OH*) and catalyzing the conversion of adsorbed substances to O_2. When substances are adsorbed on the active sites (*), the conversion reaction from basic substances (O*, OH*) and intermediates (OOH*) to O_2 continues on the active sites, and the route is divided into the following four steps:[67]

$$* + OH^- \rightarrow OH^* + e^- \quad (6)$$

$$OH^* + OH^- \rightarrow O^* + H_2O + e^- \quad (7)$$

$$O^* + OH^- \rightarrow OOH^* + e^- \quad (8)$$

$$OOH^* + OH^- \rightarrow * + O_2 + H_2O + e^- \quad (9)$$

$$\text{Overall: } 4OH^- \rightarrow O_2 + 2H_2O + 4e^- \quad (10)$$

In the process of the OER, NiFeCo-P/NF accelerated the transformation of H_2O molecules into OH– and OH*, and at the same time, phosphidizating treatment enhanced the adsorption and activation of O-containing intermediate species,[68] and contribute to the deprotonation step of the active sites from –OOH* to –OO* in the process of the OER.[69] In addition, transition metal phosphides have excellent conductivity, which can provide a conductive support for the active sites, thus promoting electron transfer.[34,39] To sum up, the phosphate group enhances the adsorption capacity and interfacial proton transfer kinetics, and the excellent conductivity of NiFeCo-P/NF improves the catalytic activity of the NiFeCo-P/NF electrode.

Conclusions

To sum up, a ZIF-67-derived NiFeCo-P nano-array was successfully prepared by three simple steps: impregnation, hydrothermal reaction and phosphidizating calcination, and showed higher OER activity in an alkaline medium than the recently reported OER electrocatalysts. Specifically, the NiCoFe-P/NF electrode only needs a low overpotential of 251 mV to reach the current density of 50 mA cm^{-2} of the OER and a small Tafel slope of 25.24 mV dec^{-1}. The high OER activity can be attributed to its open nano-array network, the synergistic effect of mixed metals and the influence of phosphidizating. This work also shows an exciting way to explore various applications of using MOFs as an interesting starting material for the manufacture of ideal LDH nanosheet arrays.

Conflicts of interest

There are no conflicts to declare.

Acknowledgements

This work is supported by the Natural Science Foundation of Shandong Province (ZR2021ME169, ZR2020KE020).

Notes and references

1 S. Gouadria, M. Abudllah, Z. Ahmad, P. John, M. U. Nisa, S. Manzoor, S. Aman, M. N. Ashiq and M. I. Ghori, *Ceram. Int.*, 2023, **49**, 4281–4289.
2 A. Z. Alhakemy, A. M. Elseman, M. G. Fayed, A. B. A. A. Nassrf, A. E.-H. Kashyoutf and Z. H. Wen, *Ceram. Int.*, 2022, **48**, 5442–5449.
3 H. N. Dhandapani, D. Mahendiran, A. Karmakar, P. Devi, S. Nagappan, R. Madhu, K. Bera, P. Murugan, B. R. Babu and S. Kundu, *J. Mater. Chem. A*, 2022, **10**, 17488.
4 X.-W. Lv, Q.-H. Kong, X.-L. Song, Y.-P. Liu and Z.-Y. Yuan, *Inorg. Chem. Front.*, 2022, **9**, 6182.
5 C. Chen, R. D. Xu, X. B. Wang, W. H. Jiang, S. Y. Feng and A. Ju, *Ceram. Int.*, 2021, **47**, 25350–25362.
6 Z. O. Owidah, S. Aman, M. Abdullah, S. Manzoor, A. M. Fallatah, M. M. Ibrahim, T. A. S. Elnasr and M. Z. Ansari, *Ceram. Int.*, 2023, **49**, 5936–5943.
7 D. M. Morales, M. A. Kazakova, S. Dieckhöfer, A. G. Selyutin, G. V. Golubtsov, W. Schuhmann and J. Masa, *Adv. Funct. Mater.*, 2022, **30**, 1905992.
8 M. Feng, J. L. Huang, Y. Peng, C. R. Huang, X. Yue and S. M. Huang, *ACS Nano*, 2022, **16**, 13834–13844.
9 Q. M. Chen, N. Gong, T. R. Zhu, C. Y. Yang, W. C. Peng, Y. Li, F. B. Zhang and X. B. Fan, *Small*, 2022, **18**, 2105696.

10 L. M. Yang, F. Ru, J. Z. Shi, T. Yang, C. Y. Guo, Y. F. Chen, E. H. Wang, Z. T. Du, K.-C. Chou and X. M. Hou, *Ceram. Int.*, 2023, **49**, 659–668.
11 A. Mariappan, R. K. Dharman and T. H. Oh, *Ceram. Int.*, 2023, **49**, 29984–29990.
12 X. Peng, Y. J. Yan, X. Jin, C. Huang, W. H. Jin, B. Gao and P. K. Chu, *Nano Energy*, 2020, **78**, 105234.
13 Y. J. Zhang, H. Xu and S. Y. Ma, *Dalton Trans.*, 2023, **52**, 9077.
14 L. Lv, Z. X. Yang, K. Chen, C. D. Wang and Y. J. Xiong, *Adv. Energy Mater.*, 2019, **9**, 1803358.
15 X. R. Zhang, X.-R. Shi, P. J. Wang, Z. Y. Bao, M. R. Huang, Y. N. Xu and S. S. Xu, *Dalton Trans.*, 2023, **52**, 6860.
16 Y.-L. Wang, T.-H. Yang, S. Yue, H.-B. Zheng, X.-P. Liu, P.-Z. Gao, H. Qin and H.-N. Xiao, *ACS Appl. Mater. Interfaces*, 2023, **15**, 11631–11641.
17 H. J. Zhang, X. P. Li, A. Hähnel, V. Naumann, C. Lin, S. Azimi, S. L. Schweizer, A. W. Maijenburg and R. B. Wehrspohn, *Adv. Funct. Mater.*, 2018, **28**, 1706847.
18 P. Wang, J. Qi, X. Chen, C. Li, W. P. Li, T. H. Wang and C. H. Liang, *ACS Appl. Mater. Interfaces*, 2020, **12**, 4385–4395.
19 Z. Yang, Y. Lin, F. X. Jiao, J. H. Li, J. L. Wang and Y. Q. Gong, *J. Energy Chem.*, 2020, **49**, 189–197.
20 M. Li, X. H. Deng, Y. Liang, K. Xiang, D. Wu, B. Zhao, H. P. Yang, J.-L. Luo and X.-Z. Fu, *J. Energy Chem.*, 2020, **50**, 314–323.
21 J. Z. Li, C. Chen, Z. P. Lv, W. S. Ma, M. Wang, Q. Li and J. Dang, *J. Mater. Sci. Technol.*, 2023, **145**, 74–82.
22 Z.-S. Fan, Y. V. Kaneti, S. Chowdhury, X. H. Wang, M. R. Karim, I. A. Alnaser and F.-B. Zhang, *Chem. Eng. J.*, 2023, **462**, 142094.
23 S. Wang, W. H. Xie, P. Wu, G. Y. Lin, Y. Cui, J. W. Tao, G. F. Zeng, Y. H. Deng and H. B. Qiu, *Nat. Commun.*, 2022, **13**, 6673.
24 S. Chowdhury, N. L. Torad, M. Godara, A. A. M. El-Amir, G. Gumilar, A. Ashok, M. R. Karim, I. A. Alnaser, W. Chaikittisilp, N. Ray, Y. Yamauchi and Y. V. Kaneti, *Chem. Eng. J.*, 2024, **480**, 147990.
25 K. Sathiyan, A. Dutta, V. Marks, O. Fleker, T. Zidki, R. D. Webster and A. Borenstein, *NPG Asia Mater.*, 2023, **15**, 18.
26 P. Cheng, X. H. Wang, J. Markus, M. A. Wahab, S. Chowdhury, R. J. Xin, S. M. Alshehri, Y. Bando, Y. Yamauchi and Y. V. Kaneti, *J. Colloid Interface Sci.*, 2023, **638**, 220–230.
27 Y. J. Sun, L. W. Zheng, Y. Yang, X. Qian, T. Fu, X. W. Li, Z. Y. Yang, H. Yan, C. Cui and W. H. Tan, *Nano-Micro Lett.*, 2020, **12**, 103.
28 W. R. Cheng, X. Zhao, H. Su, F. M. Tang, W. Che, H. Zhang and Q. H. Liu, *Nat. Energy*, 2019, **4**, 115–122.
29 Z. K. Wang, S. Y. Wang, L. X. Ma, Y. J. Guo, J. Sun, N. Zhang and R. B. Jiang, *Small*, 2021, **17**, 2006770.
30 J. X. Chen, Q. W. Long, K. Xiao, T. Ouyang, N. Li, S. Y. Ye and Z.-Q. Liu, *Sci. Bull.*, 2021, **66**, 1063–1072.
31 X. Wu, L. He and X. Y. Wang, *Ceram. Int.*, 2021, **47**, 25755–25762.
32 L. Yang, G. L. Zhu, H. Wen, X. Guan, X. Sun, H. Feng, W. L. Tian, D. C. Zheng, X. W. Cheng and Y. D. Yao, *J. Mater. Chem. A*, 2019, **17**, 8771.
33 Y. M. Ma, D. Y. Liu, H. Wu, M. T. Li, S. J. Ding, A. S. Hall and C. H. Xiao, *ACS Appl. Mater. Interfaces*, 2021, **13**, 26055–26063.
34 X. Wu, L. He and X. Y. Wang, *Ceram. Int.*, 2021, **47**, 25755–25762.
35 L. Yu, H. Q. Zhou, J. Y. Sun, I. K. Mishra, D. Luo, F. Yu, Y. Yu, S. Chen and Z. F. Ren, *J. Mater. Chem. A*, 2018, **6**, 13619.
36 W. S. Mai, Q. Cui, Z. Q. Zhang, K. K. Zhang, G. Q. Li, L. H. Tian and W. Hu, *ACS Appl. Energy Mater.*, 2020, **3**, 8075–8085.
37 B. Fei, Z. F. Yao, D. P. Cai, J. H. Si, Q. T. Wang, Q. D. Chen, B. S. Sa, K. P. Peng and H. B. Zhan, *Energy Storage Mater.*, 2020, **25**, 105–113.
38 Z. P. Wang, J. H. Zhang, Q. Y. Yu, H. Y. Yang, X. Chen, X. Yuan, K. Huang and X. L. Xiong, *Chem. Eng. J.*, 2021, **410**, 128366.
39 C. W. Wan, J. Jin, X. Y. Wei, S. Z. Chen, Y. Zhang, T. L. Zhu and H. X. Qu, *J. Mater. Sci. Technol.*, 2022, **124**, 102–108.
40 Y. Y. Li, H. R. Guo, Y. Zhang, H. T. Zhang, J. Y. Zhao and R. Song, *J. Mater. Chem. A*, 2022, **10**, 18989.
41 R. Guo, Y. He, R. C. Wang, J. H. You, H. J. Lin, C. Chen, T. S. Chan, X. W. Liu and Z. W. Hu, *Inorg. Chem. Front.*, 2022, **9**, 6182.
42 F. Nie, Z. Li, X. P. Dai, X. L. Yin, Y. H. Gan, Z. H. Yang, B. Q. Wu, Z. T. Ren, Y. H. Cao and W. Y. Song, *Chem. Eng. J.*, 2022, **431**, 134080.
43 K. Chen, Y.-H. Cao, S. Yadav, G.-C. Kim, Z. Han, W. M. Wang, W.-J. Zhang, V. Dao and I.-H. Lee, *Chem. Eng. J.*, 2023, **463**, 142396.
44 S. R. Xu, X. Yu, L. Luo, W. J. Li, Y. S. Du, Q. Q. Kong and Q. Wu, *Nano Res.*, 2022, **15**, 4942–4949.
45 C. J. Xuan, J. Wang, W. W. Xia, J. Zhu, Z. K. Peng, K. D. Xia, W. P. Xiao, H. L. L. Xin and D. L. Wang, *J. Mater. Chem. A*, 2018, **6**, 7062–7069.
46 Y. J. Lee and S.-K. Park, *Small*, 2022, **18**, 2200586.
47 J. Wang, G. C. Lv and C. Wang, *Appl. Surf. Sci.*, 2021, **570**, 151182.
48 H. Li, Y. M. Du, Y. L. Fu, C. Y. Wu, Z. Y. Xiao, Y. R. Liu, X. M. Sun and L. Wang, *Int. J. Hydrogen Energy*, 2020, **45**, 565–573.
49 X. L. Hu, T. X. Yang, Z. G. Yang, Z. Y. Li, R. H. Wang, M. Li, G. S. Huang, B. Jiang, C. H. Xua and F. S. Pan, *J. Mater. Sci. Technol.*, 2022, **115**, 19–28.
50 X. Y. Wang, Y. X. Tuo, Y. Zhou, D. Wang, S. T. Wang and J. Zhang, *Chem. Eng. J.*, 2021, **403**, 126297.
51 H. Luo, J. Liang, J. L. Zhou, Z. Yin, Y. Zhang and X. B. Liu, *New J. Chem.*, 2022, **46**, 7999.
52 J. H. Li, L. L. Wang, H. J. He, Y. Q. Chen, Z. R. Gao, N. Ma, B. Wang, L. L. Zheng, R. L. Li, Y. J. Wei, J. Q. Xu, Y. Xu, B. W. Cheng, Z. Yin and D. Ma, *Nano Res.*, 2022, **15**, 4986–4995.
53 J. Q. Wang, D. T. Tran, K. Chang, S. Prabhakaran, J. H. Zhao, D. H. Kim, N. H. Kim and J. H. Lee, *Nano Energy*, 2023, **111**, 108440.
54 K. Chang, D. T. Tran, J. Q. Wang, K. X. Dong, S. Prabhakaran, D. H. Kim, N. H. Kim and J. H. Lee, *Appl. Catal., B*, 2023, **338**, 123016.
55 L. Y. Hu, L. L. Tian, X. Ding, X. Wang, X. S. Wang, Y. Qin, W. L. Gu, L. Shi and C. Z. Zhu, *Inorg. Chem. Front.*, 2022, **9**, 5296.

56 W. Zhang, H. J. Yan, Y. Liu, D. X. Wang, Y. Q. Jiao, A. P. Wu, X. W. Wang, R. H. Wang and C. G. Tian, *J. Mater. Chem. A*, 2023, **11**, 15033–15043.
57 J. T. Ding, T. Fan, K. Shen and Y. W. Li, *Appl. Catal., B*, 2021, **292**, 120174.
58 G. Liu, D. Y. He, R. Yao, Y. Zhao and J. P. Li, *Electrochim. Acta*, 2017, **253**, 498–505.
59 Q. H. Yang, Y. Y. Fu, W. H. Liao, Y. Q. Zhang, M. Qian, H. J. Dai, X. F. Tong and T. Y. Chen, *Int. J. Hydrogen Energy*, 2021, **46**, 39736–39742.
60 X. B. Wang, J. L. Wang, J. Liao, L. Wang, M. Li, R. D. Xu and L. J. Yang, *Appl. Surf. Sci.*, 2022, **602**, 154287.
61 A. Meena, P. Thangavel, D. S. Jeong, A. N. Singh, A. Jana, H. Im, D. A. Nguyen and K. S. Kim, *Appl. Catal., B*, 2022, **306**, 121127.
62 F. S. Wen, T. Zhang, W. L. Liu, Y. J. Li, L. Pang, X. L. Huang and D. Liu, *Colloids Surf., A*, 2022, **646**, 128929.
63 W. Z. Yuan, T. F. Jiang, X. Q. Fang, Y. Fan, S. Qian, Y. Y. Gao, N. Y. Cheng, H. G. Xue and J. Q. Tian, *Chem. Eng. J.*, 2022, **439**, 135743.
64 F.-S. Zhang, J.-W. Wang, J. Luo, R.-R. Liu, Z.-M. Zhang, C.-T. He and T.-B. Lu, *Chem. Sci.*, 2018, **9**, 1375.
65 Y. Li, Y. Y. Wu, H. R. Hao, M. K. Yuan, Z. Lv, L. L. Xu and B. Wei, *Appl. Catal., B*, 2022, **305**, 121033.
66 A. Dutta and N. Pradhan, *J. Phys. Chem. Lett.*, 2017, **8**, 144–152.
67 M. Bajdich, M. García-Mota, A. Vojvodic, J. K. Nørskov and A. T. Bell, *J. Am. Chem. Soc.*, 2013, **135**, 13521–13530.
68 B. B. Yuan, F. Z. Sun, C. Q. Li, W. Huang and Y. Q. Lin, *Electrochim. Acta*, 2019, **313**, 91–98.
69 C. Z. Yang, C. Laberty-Robert, D. Batuk, G. Cibin, A. V. Grimaud, V. Pimenta, W. Yin, L. T. Zhang, J.-M. Tarascon and A. Grimaud, *J. Phys. Chem. Lett.*, 2017, **8**, 3466.